Investigation of Structural and Optical Properties of Amorphous-Crystalline Phase Transition of As$_{40}$S$_{45}$Se$_{15}$ Thin Films

E.R. Shaaban^{a,*}, M.Y. Hassaan^{b}, M.G. Moustafa^{b,c}, Ammar Qasem^{b}, G.A.M. Ali^{d}
and E.S. Yousef^{e,f}

^{a}Physics Department, Faculty of Science, A1-Azhar University, Assiut 71542, Egypt

^{b}Physics Department, Faculty of Science, Al-Azhar University, Nasr City 11884, Cairo, Egypt

^{c}Physics Department, College of Science. & Arts, Jouf University, Qurayat, P.O. 756, Saudi Arabia

^{d}Chemistry Department, Faculty of Science, A1-Azhar University, Assiut 71542, Egypt

^{e}Physics Department, Faculty of Science, King Khalid University, P.O. Box 9004, Abha, Saudi Arabia

^{f}Research Center for Advanced Materials Science (RCAMS), King Khalid University,

Abha 61413, P.O. Box 9004, Saudi Arabia

In the present work, the influence of heat treatment on the structural and optical properties of amorphous As$_{40}$S$_{45}$Se$_{15}$ chalcogenide thin films is investigated. The structural analyses of the thin films have been studied via X-ray diffraction technique. The X-ray diffraction studies exhibit that the crystallinity improves with increase of the thermal annealing temperature from inset temperature to maximum crystallization temperature. On the other hand, the optical constants of the as-prepared and annealed As$_{40}$S$_{45}$Se$_{15}$ samples were computed via envelope method. Then, the optical band gap of as-prepared and annealed samples as a function of photon energy in the wavelength range 400–2500 nm were investigated. The optical band gap was successfully calculated by Tauc's relation which exhibits the indirect transitions for the as-prepared and annealed samples under onset temperature and allowed direct transition for annealed samples at and above inset temperature. The dispersion parameters of the films were computed via the single oscillator model proposed by the Wemple–DiDomenico relation. The static refractive indices (both linear and non-linear) optical susceptibility $\chi^{(1)}$, $\chi^{(3)}$, and then non-linear refractive indices were also computed. Starting with dielectric constants (ε_r and ε_i) the loss tangent and volume/surface energy loss functions were computed. Also the inter-band transition strength $J_{cv}(E)$ for the dipole selection rules for the transitions was discussed.

1. Introduction

In the past years, the progress in science has occurred fundamentally with the discovery of new materials. Characterization is an important and essential step in the development of strange materials. The complete characterization of any material includes phase analysis, compositional characterization, structural and surface characterization, which have a strong bearing on the properties of materials. Then, chalcogenide materials and their thin films are the key elements of continued technological improvements made in the fields of photonic, optoelectronic, and magnetic devices. Many applications for chalcogenide glasses have been reported, for example, in wireless communications, semiconductor devices, telecommunications, integrated circuits, transistors, solar cells, rectifier, light-emitting diodes, photoconductors, magneto-optic memories, audio and video systems, smart windows, computer chips [1, 2]. These applications are possible due to their smaller phonon energies as compared to oxide glasses and their better-infrared transmission [3, 4]. Additionally, the light processes display the possibility of using non-crystalline semiconductors for wide technological applications such as xerography switching, photolithographic process, filters, modulators, scanning near field microscopy/spectroscopy, and more recently as reversible phase change optical recorders [5–11]. Many physical deposition techniques are available for the growth of As–S–Se thin films [12, 13]. Several reports debated the effect of growth conditions on the properties of As–S–Se thin films for using in different technological applications. In addition, more efforts have been made to develop the mathematical formulation describing both the reflectance and the transmittance of many optical systems [8, 13–20]. However, there are no detailed studies on the structural and optical properties of thermally deposited As$_{40}$S$_{45}$Se$_{15}$ thin films. Few reports are available on this [13, 21]. The investigation of chalcogenide thin films in the binary and ternary systems of As–S–Se is suitable for utilizing optical devices. The interest in such glasses has been previously discussed [8, 21, 22].

*corresponding author; e-mail: esam_ramadan2008@yahoo.com

The aim of this work is to study the effect the thermal processes on the optical properties of $As_{40}S_{45}Se_{15}$ thin films, based on a proposal from Swanepoel to determine the optical constants employing only the transmission spectra. The renowned Swanepoel's method has been inserted to deduce the refractive index, film thickness, the extinction coefficient k, and then the rest of the optical parameters and constants in the transparent region. The optical absorption data shows that the indirect transitions dominate for as-prepared film and annealed temperatures between glass transition T_g and any temperature under an onset temperature T_c while the allowed direct transition dominate around and above T_c. The dispersion parameters are discussed via single-oscillator Wemple–DiDomenico model [23]. The variation of the optical band-gap and single oscillator energy with different annealed temperatures and non-linear refractive index are discussed according to two models that are mentioned below.

2. Experimental methods

In this work, the bulk alloy of $As_{40}S_{45}Se_{15}$ was prepared by the usual melt quench technique. Highly pure (99.999%) As, S, and Se elements, (5N, Aldrich and Sigma chemical company) were weighed according to their atomic percentages and placed together in a pre-cleaned and outgassed silica ampoule, which was evacuated to a pressure of about 10^{-4} Pa and then sealed. The synthesis was performed in a programmable rocking furnace and slowly heated up to approximately 1000 °C with the temperature ramp about 5 °C/min, for about 24 h. The ampoule was inverted at regular time intervals ($\approx$ 1 h) during the melting process so that the amorphous solid will be homogeneous and isotropic. After the synthesis, the melt was quenched rapidly in ice water to obtain $As_{40}S_{45}Se_{15}$ glassy alloy. Then the solid was broken along its natural stress line into smaller pieces suitable for grinding. The calorimetric measurement of $As_{40}S_{45}Se_{15}$ was carried out in a differential scanning calorimeter Shimadzu 50 with an accuracy of ±0.1 K. The calorimeter was calibrated, for heating rate, using well-known melting temperatures and melting enthalpies of zinc and indium supplied with the instrument. Twenty mg powdered sample, crimped into aluminum pans was scanned at different heating rate ($\beta = 10$ K/min). The temperatures of the glass transition, T_g, the crystallization extrapolated onset, T_{in} and the crystallization peak, T_p were determined with an accuracy of ±1 K.

X-ray powder diffraction (XRD) Philips diffractometry (1710), with Cu K_{α_1} radiation ($\lambda = 1.54056$ Å) have been used to examine the structure of the as prepared and annealed $As_{40}S_{45}Se_{15}$ glassy alloy, as deposited and annealed thin films. The data collection was performed by step scan mode, in a 2θ range between 5° and 80° with step-size of 0.02° and step time of 0.6 s. Pure silicon $\approx$ Si 99.9999% was used as an internal standard.

$As_{40}S_{45}Se_{15}$ thin films were prepared by thermal evaporation technique via a coating unit (Denton Vacuum DV 502 A) under high vacuum conditions (10^{-7} mbar). The substrates utilized for deposition were carefully cleaned using ultrasonic hot bath distilled water and pure alcohol before the evaporation process started. The thickness of the as-deposited films studied is mostly about 500 nm in order to avoid the effect of film thickness. During the deposition process, the substrates were kept at room temperature 300 K and the deposition rate was adjusted at 10 Å/s. The substrates were rotated at slow speed 5 rev/min to obtain a homogeneous and smooth film. During evaporation process, the thickness of the produced films was monitored using FTM6 thickness monitor. The structure and phase of the as-deposited film and annealed films in a vacuum of (10^{-3} Torr) with five different temperatures 370, 380, 390, 400, and 410 K respectively, for a fixed time (30 min) and then cooled down to room temperature. The transmittance and reflectance spectra for as-deposited and annealed films were obtained by a double-beam computer-controlled spectrophotometer (UV-2101, Shimadzu) at normal light incidence in the range of wavelength from 400 to 2500 nm.

3. Results and discussion

3.1. Structural characterization

The experimental data of the differential scanning calorimetry (DSC) for the $As_{40}S_{45}Se_{15}$ powder at a heating rate of 10 K/min is presented in Fig. 1a. One can notice that three characteristic phenomena are evident in the same range of temperature: only one glass transition temperature T_g, onset crystallization temperature T_c, and the peaks of crystallization T_p. The thermal annealing was applied to $As_{40}S_{45}Se_{15}$ thin films at five various annealed temperatures (see the red points in Fig. 1a) 370, 380, 390, 400, and 410 K, with a heating rate of 10 K/min at a fixed time (30 min) under nitrogen gases in the range of glass transition temperature and maximum crystallization temperature of the investigated samples. The peak intensities are computed by the distribution of atoms within the lattice. Then, XRD pattern is the fingerprint of periodic atomic arrangements in a given material. Figure 1b presents the XRD that is used to observe the transformation from amorphous to gradually crystalline thin films. The as-prepared thin film and annealed others at 370 and 380 K are typically still in the amorphous state. The studied thin films start to convert from amorphous state to crystalline state with increase of the annealing temperatures at 390 K and the sharpness intensity of peaks increases with increase of the annealing temperatures after that. This means that the rearrangement of atoms and elimination the crystal defects in the thin film increases with increase in the heat treatment. The patterns of XRD of the annealed films exhibit a presence of the main $As_2(Se, S)_3$ phase. The dominant crystalline phase is $As_2(Se, S)_3$ with crystal structure with a unit cell defined by $a = 1.19$ nm, $b = 0.98$ nm, and $c = 0.426$ nm, and also $\alpha = \gamma = 90°$, $\beta = 90.17°$, and calculated density, measured density, and volume of cell

TABLE I

The X-ray data, crystallite size D, strain ε and dislocation density δ for the dominant monoclinic phase observed in the $As_{40}S_{45}Se_{15}$ thin films annealed at various temperatures.

| T [K]	d_{exp} [Å]	d_{stand} [Å]	(hkl)	D [nm]	$\varepsilon \times 10^{-4}$	$\delta \times 10^{15}$ [m^{-2}]
	3.05	3.04	(110)	10.23	3.8	9.50
	4.12	4.11	(0 3 0)	8.14	1.2	15.1
390	4.77	4.77	(0 0 2)	11.29	1.8	7.84
	3.52	3.51	(1 1 0)	11.87	4.3	7.09
	2.12	2.12	(1 −1 1)	10.27	5.8	9.48
	5.19	5.19	(210)	11.44	5.1	7.64
	4.65	4.66	(3 0 0)	9.32	3.4	10.15
400	3.12	3.12	(2 2 −3)	11.96	2.9	6.99
	2.44	2.45	(1 0 −2)	12.07	8.5	6.86
	2.39	2.39	(−2 2 1)	11.92	3.9	7.03
	4.87	4.87	(020)	12.09	1.1	6.84
	2.82	2.83	(2 2 1)	10.14	2.4	9.72
410	1.76	1.77	(0 5 1)	12.56	4.6	6.33
	1.70	1.70	(−2 3 2)	12.59	4.1	6.31
	1.51	1.51	(−5 5 0)	13.02	1.9	5.90
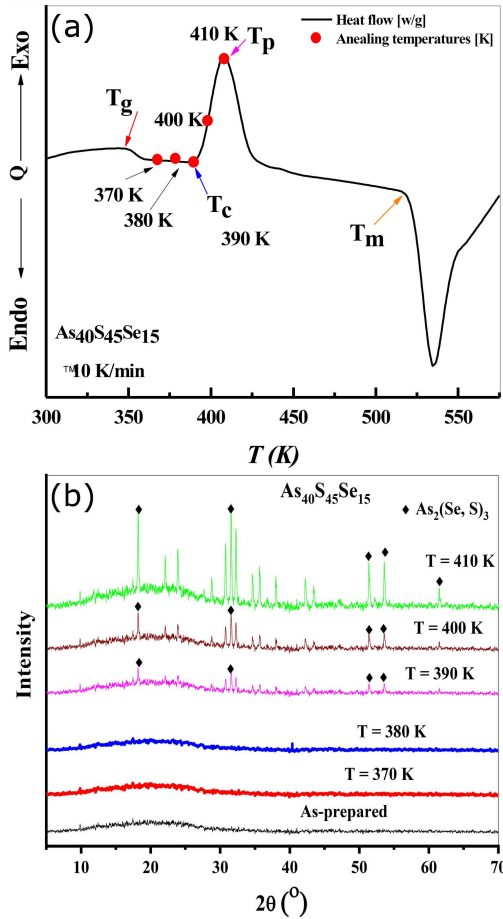
Fig. 1. DSC thermograms for bulk $As_{40}S_{45}Se_{15}$ glass alloy (a) and X-ray diffraction patterns of $As_{40}S_{45}Se_{15}$ thin films of as-prepared and annealed at various temperatures (b).

equal to 4.60 g/cm^3, 4.50 g/cm^3, and 493.48 cm^3 according to card No.: 00-040-0469 [24]. For thin films annealed at 390, 400, and 410 it is clear that examination of the film shows some prominent peaks related to crystalline phases indicating the crystallization process. The corresponding Miller indices hkl for the dominant phase are determined on the basis of the best agreement between observed of inter-planar spacing d_{exp} and those of Joint Committee on Powder Diffraction Standards (JCPDS), d_{stand} as presented in Table I, for the dominant phase that appears with increase in the annealing temperatures.

The crystallite size D, dislocation density δ, and the micro-strain (ε) can be computed as a function of annealing temperature, which plays an important role in many properties such as mechanical properties and thermal stability. The average particle size of the crystalline phase was computed according to Scherrer's equation [25]:

$$D = \frac{K\lambda}{\beta \cos\theta}, \qquad (1)$$

where λ is the X-ray wavelength in nm, β is the full width at half maximum (FWHM) of the diffraction peak, and θ is the diffraction angle. The Scherrer constant K is the grain shape factor and is assigned a value of 0.94. On the other hand, the dislocation density determined via the relation [26, 27]:

$$\delta = \frac{1}{D^2}. \qquad (2)$$

Furthermore, the strain value is also attached to the lattice mismatch and may be computed from the subsequent equation [28]:

$$\varepsilon = \left(\frac{\lambda}{D \cos\theta} - \beta \right) \frac{1}{\tan\theta}. \qquad (3)$$

The computed values of D, δ, and ε are listed in Table I. The values of the crystallite size are increased whereas the dislocation density and strain are decreased with increasing annealing temperatures. This may be attributed to decreasing lattice defects among the grain boundaries [29, 30].

3.2. Optical properties

Investigation of the optical properties of chalcogenide materials is very important for the estimation of their electronic band structure as well as other optical parameters, such as optical energy gap and tail energy and computation of essential optical constant, such as refractive index and extinction coefficient. For crystalline semiconductors, the associated optical absorption spectrum terminates suddenly at the fundamental gap, while in amorphous semiconductors a tail in the optical absorption spectrum encroaches into the gap region. This tail in the optical absorption spectrum, arising as a consequence of the tail and gap states, makes the optical gap of an amorphous semiconductor difficult to deduce experimentally. In this work, we will study the optical properties as follows.
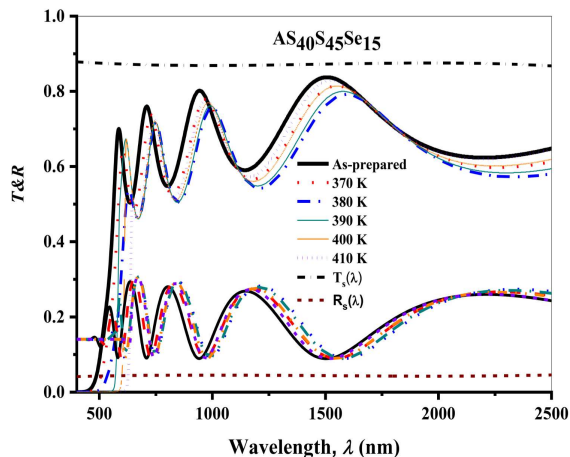

Fig. 2. The transmittance and reflectance spectra for $As_{40}S_{45}Se_{15}$ thin films annealed at various temperatures.

3.2.1. Interference fringes in transmittance spectra

The optical properties were investigated for as-prepared and annealed $As_{40}S_{45}Se_{15}$ thin films via optical transmittance ($T(\lambda)$) and the reflectance ($R(\lambda)$) data of wavelength range of 400–2500 nm. Figure 2 presents spectra of $T(\lambda)$ and $R(\lambda)$ for as-prepared and annealed $As_{40}S_{45}Se_{15}$ thin films. The thickness of the as-prepared and annealed samples were computed according to Swanepoel's method, which is based on the idea of Manifacier et al. [14] of creating upper and lower envelopes of the transmittance spectrum which showed the construction of the two envelopes $T_M(\lambda)$, $T_m(\lambda)$ and then the geometric mean

$$T_\alpha = \sqrt{T_M(\lambda)T_m(\lambda)}. \quad (4)$$

3.2.2. Envelope construction

In all investigated thin films, the two envelopes construction $T_M(\lambda)$ and $T_m(\lambda)$ are expressed by the subsequent two functions, respectively

$$T_{M_j} = T_0 + A_1 \exp\left(-\frac{\lambda_j}{t_1}\right) + A_2 \exp\left(-\frac{\lambda_j}{t_2}\right), \quad (5)$$

$$T_{m_j} = T_0 + A_1 \exp\left(\frac{\lambda_j}{t_1}\right) + A_2 \exp\left(-\frac{\lambda_j}{t_2}\right), \quad (6)$$

where the constants of each equation are different from the other equation constants and vary from one thin film to another. Here T_{M_j} and T_{m_j} are the transmission maximum and the corresponding minimum at a certain wavelength. Alternatively, one of these values is an empirical interference extreme and the other one is derived from the corresponding envelope. Both envelopes were computer-generated via the program Origin version 7 (Origin-Lab Corp.). The values of these constants are presented in Table II. $T_M(\lambda)$ and $T_m(\lambda)$ are illustrated in Fig. 3 and the values are listed in Table III.

3.2.3. Estimation refractive index of the substrate

The refractive index of the film substrate must first be computed via the subsequent relation [30]:

$$s_j = (T_{s_j})^{-1} + \sqrt{(T_{s_j})^{-1} - 1}, \quad (7)$$

where T_s is the transmittance of the glass substrate which has been defined by the subsequent function:

$$T_{s_j} = [A + B_j + C_j^2 + D_j^3], \quad (8)$$

where j is a number that refers to a specific wavelength and the values of the constants that appear in Eq. (8), namely A, B, C, and D, are equal to 0.901414, 8.02369×10^{-5}, 6.13838×10^{-8}, and 1.38877×10^{-11}, respectively.

3.2.4. Estimation of crude refractive index

The crude refractive index (n_e) of the as-prepared and annealed films under investigation can be computed based on envelope method via transmission spectrum proposed by Swanepoel [31, 32]. The values of n_e can be computed at any wavelength via the relation

$$n_e = [N + (N^2 - s_j^2)^{1/2}]^{1/2}, \quad (9)$$

where

$$N = 2s_j \frac{T_{M_j} - T_{m_j}}{T_{M_j} T_{m_j}} + \frac{s_j^2 + 1}{2}, \quad (10)$$

where s_j is the refractive index of the glass substrate. Values of crude refractive index, $n_e \equiv n_1$ for as-prepared and different annealed temperatures of thin films under investigation, are computed and listed in Table III.

3.2.5. Determination of the crude and accuracy films thickness

Values of n_e at any adjacent maximal (or minimal), that have been computed by Eq. (9) are used to deduce crude thickness film, $d_{\mathrm{crude}} \equiv d_1$. If n_{e1} and n_{e2} are the refractive indices of two adjacent maxima or minima at wavelengths λ_{e1} and λ_{e2}, then the crude thickness of the film is expressed as [12]:

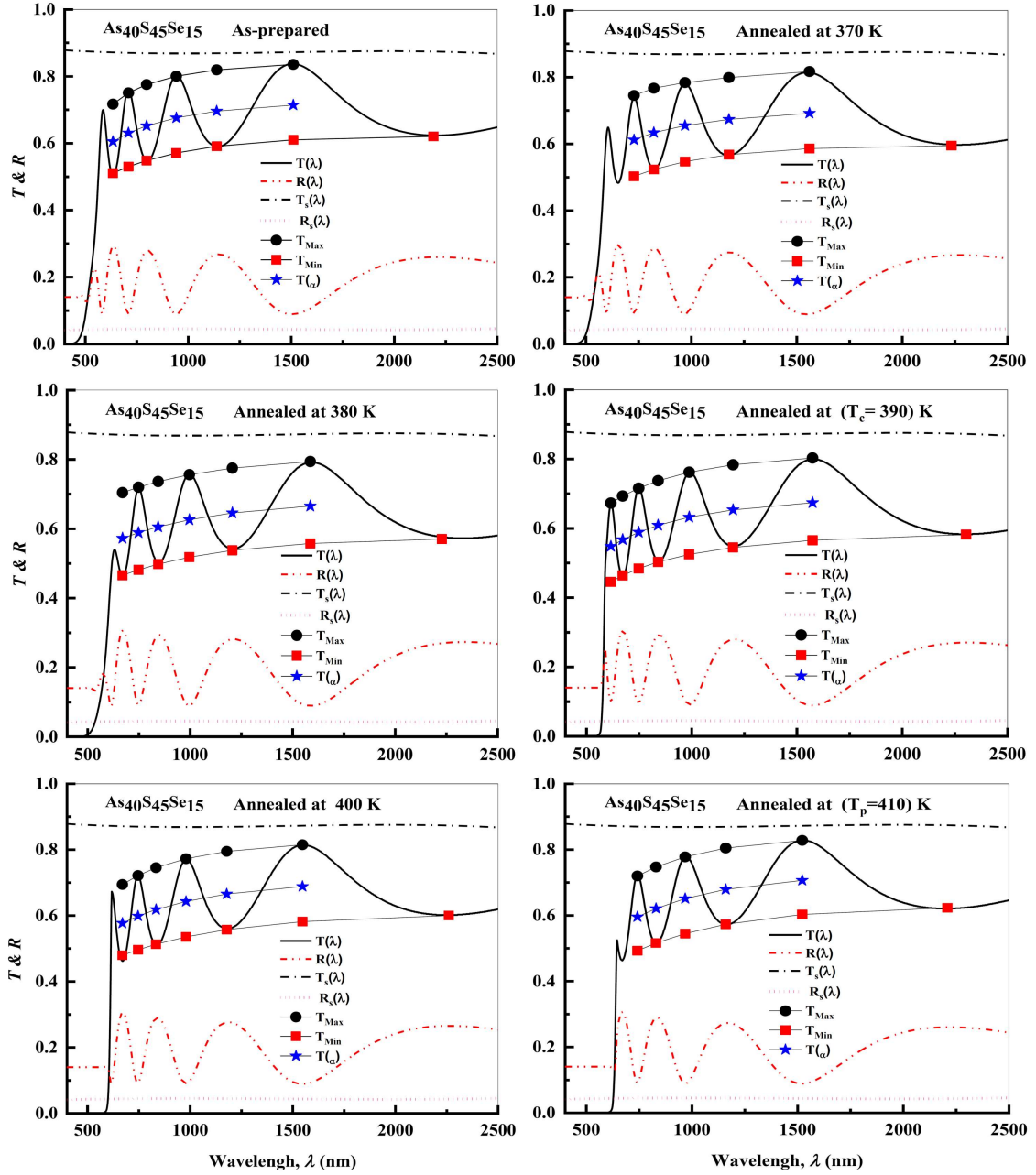$$d_1 = \frac{\lambda_{e1}\lambda_{e2}}{2}(\lambda_{e1}n_{e2} - \lambda_{e2}n_{e1})^{-1}. \quad (11)$$

Fig. 3. Variation of envelope construction of the typical spectral transmittance and reflectance vs. wavelength for $As_{40}S_{45}Se_{15}$ thin films annealed at various temperatures.

TABLE II

The constants relate to both the maximum and minimum envelopes of transmission spectra for investigated thin films.

T [K]	T_{M_j} obtained with Eq. (5)					T_{m_j} obtained with Eq. (6)				
	T_o	A_1	t_1	A_2	t_2	T_o	A_1	t_1	A_2	t_2
as-prep.	0.845	-0.544	372.4	-14.14	102.4	0.623	-0.276	398.3	-0.276	398.3
370	0.844	-372.5	72.49	-0.220	742	0.596	-0.320	379.1	-0.320	379.1
380	0.810	-0.209	485.8	-0.209	485.8	0.575	-0.209	500.7	-0.209	500.7
390	0.817	-0.392	470.2	-0.595	225.1	0.590	-0.817	211.5	-0.249	674.3
400	0.829	-1.260	176.3	-0.505	429.1	0.607	-0.221	537.3	-0.221	537.3
410	0.841	-0.520	344.3	-0.520	344.3	0.629	-0.330	470.1	-0.330	470.1

TABLE III

Values of the wavelength λ of the incident photon, the two envelopes T_M and T_m for the $As_{40}S_{45}Se_{15}$ three thin films (as-prepared, 370, 380, 390, 400 and 410 K). The calculated values of the refractive index and film thickness are based on the envelope method.

T [K]	λ_e [nm]	T_M	T_m	S	n_e	d_1	m_o	m	d_2	n_2
as-prep.	634	0.717	0.511	1.532	2.53	580.31	4.173	4	499.67	2.67
	710	0.751	0.530	1.536	2.52	530.18	3.714	3.5	491.24	2.55
	798	0.776	0.549	1.540	2.59	495.51	3.275	3	477.56	2.49
	942	0.800	0.571	1.543	2.46	479.17	2.731	2.5	477.21	2.43
	1138	0.819	0.591	1.543	2.42	–	2.223	2	469.06	2.38
	1510	0.836	0.610	1.537	2.37	–	1.643	1.5	475.92	2.34
	2190	–	0.621	1.541	–	–	–	–	–	2.31
$\bar{d}_1 = 521.29$ nm, $\sigma_1 = 38.733$ nm (7.43%), $\bar{d}_2 = 481.78$ nm, $\sigma_2 = 10.36$ nm (2.15%)										
370K	728	0.745	0.502	1.537	2.64	488.77	3.479	3.5	481.39	2.65
	822	0.767	0.523	1.540	2.60	471.46	3.027	3	474.20	2.59
	970	0.784	0.547	1.543	2.53	475.38	2.500	2.5	478.50	2.53
	1178	0.799	0.567	1.543	2.47	–	2.012	2	475.58	2.48
	1560	0.817	0.586	1.536	2.43	–	1.494	1.5	480.60	2.43
	2234	–	0.594	1.543	–	–	–	–	–	2.40
$\bar{d}_1 = 478.53$ nm, $\sigma_1 = 7.411$ nm (1.55%), $\bar{d}_2 = 478.05$ nm, $\sigma_2 = 2.785$ nm (0.58%)										
380K	670	0.704	0.465	1.534	2.74	529.49	4.09	4	489.04	2.79
	748	0.720	0.481	1.538	2.69	504.31	3.61	3.5	485.34	2.71
	844	0.736	0.497	1.541	2.65	486.89	3.15	3	476.90	2.65
	996	0.756	0.518	1.543	2.60	482.15	2.61	2.5	478.15	2.58
	1206	0.774	0.537	1.542	2.55	–	2.12	2	472.07	2.52
	1586	0.794	0.557	1.535	2.50	–	1.57	1.5	475.52	2.47
	2228	–	0.570	1.543	–	–	–	–	–	2.44
$\bar{d}_1 = 500.71$ nm, $\sigma_1 = 18.55$ nm (3.7%), $\bar{d}_2 = 479.50$ nm, $\sigma_2 = 5.842$ nm (1.22%)										
390K	616	0.673	0.445	1.531	2.77	541.21	4.65	4.5	500.09	2.85
	672	0.693	0.464	1.534	2.72	544.59	4.19	4	493.60	2.77
	748	0.716	0.484	1.538	2.67	521.92	3.69	3.5	489.47	2.69
	840	0.737	0.503	1.541	2.63	495.74	3.24	3	478.66	2.62
	988	0.762	0.524	1.543	2.58	482.38	2.70	2.5	477.59	2.55
	1196	0.783	0.545	1.542	2.54	–	2.19	2	470.55	2.48
	1574	0.803	0.565	1.536	2.48	–	1.63	1.5	474.44	2.43
	2303	–	0.582	1.548	–	–	–	–	–	2.39
$\bar{d}_1 = 517.17$ nm, $\sigma_1 = 24.584$ nm (4.75%), $\bar{d}_2 = 483.48$ nm, $\sigma_2 = 10.15$ nm (1.1%)										
400K	670	0.6944	0.479	1.534	2.64	607.2	4.14	4	507.2	2.76
	746	0.721	0.496	1.538	2.62	551.9	3.69	3.5	497.2	2.67
	834	0.745	0.512	1.541	2.60	506.6	3.27	3	480.8	2.60
	980	0.772	0.535	1.543	2.56	484.5	2.74	2.5	478.2	2.51
	1178	0.794	0.557	1.543	2.51	476.1	2.24	2	468.8	2.45
	1547	0.814	0.581	1.536	2.44	–	1.66	1.5	474.1	2.38
	2260	–	0.600	1.545	–	–	–	–	–	2.34
$\bar{d}_1 = 525.30$ nm, $\sigma_1 = 48.68$ nm (9.27%), $\bar{d}_2 = 484.38$ nm, $\sigma_2 = 13.45$ nm (2.78%)										
410K	742	0.720	0.492	1.538	2.63	530.7	3.58	3.5	491.9	2.69
	830	0.747	0.516	1.541	2.59	502.6	3.14	3	480.3	2.60
	968	0.778	0.544	1.543	2.53	478.9	2.63	2.5	477.9	2.51
	1160	0.804	0.573	1.543	2.46	–	2.14	2	469.9	2.44
	1522	0.828	0.603	1.537	2.39	–	1.58	1.5	477.3	2.36
	2209	–	0.623	1.542	–	–	–	–	–	2.31
$\bar{d}_1 = 504.07$ nm, $\sigma_1 = 21.173$ nm (4.2%), $\bar{d}_2 = 479.46$ nm, $\sigma_2 = 7.127$ nm (1.49%)										

To improve the accuracy of thickness film there is a set of the order number m_o for the interference fringes which are deduced via relation [12]:

$$m_0 = \frac{2n_{e1}\bar{d}_1}{\lambda_{e1}}, \qquad (12)$$

where $n_e \equiv n_1$ and λ_{e1} are the values taken at the extreme point of the interference fringes and $\bar{d}_1$ is the average of d_{crude} from Eq. (11). Then, by taking the approximate value of m_o, a new order number m is produced where $m = 1, 2, 3\ldots$ at the maximum points in the transmission spectrum and $m = 1/2, 3/2, 5/2\ldots$ at minimum points in the transmission spectrum. After that, the accuracy of refractive index $n_{\mathrm{accurate}} \equiv n_2$ in terms of accuracy of thickness thin film, is expressed, $d_{\mathrm{accurate}} \equiv d_2$ as the subsequent relation

$$n_2 = \frac{m\lambda_{e1}}{2\bar{d}_2}, \qquad (13)$$

where $\bar{d}_2$ is the new average accuracy of thickness of thin films after rounding m_o to m. The final values of new refractive index n_2 and other mentioned values are presented in Table III. On the other hand, to compute the standard deviation values σ_i and deviation ratio p_i about the actual value for each of d_1 and d_2, we use the subsequent equation:

$$\sigma_i = \left[\frac{1}{n}\sum_1^n (d_i)^2 - (\bar{d}_i)^2\right]^{0.5},$$

$$\bar{d}_i = \frac{1}{n}\sum_1^n (d_i), \quad p_i[\%] = \frac{\sigma_i}{d_i} \times 100, \qquad (14)$$

where i is a number equal to 1 or 2 and n refers to the number of thicknesses.

3.2.6. Estimation of optical parameters

Now, the absorption coefficient α can be computed in the strong absorption region via both the empirical transmission T and reflection R spectra [33, 34]:

$$\alpha = \frac{1}{d}\ln\left(\frac{(1-R)^2 + \sqrt{(1-R)^4 + 4(TR)^2}}{2T}\right), \quad (15)$$

where d is the thickness of the films that is computed by Swanepoel's method and is almost equal to 500 nm. The variation of α versus photon energy $h\nu$ as a function of annealed temperature for $As_{40}S_{45}Se_{15}$ thin films is shown in Fig. 4a. It is clear that the absorption edge ($\alpha \geq 10^4$) shifts towards the lower photon energy with increase of annealing temperature that is related to the decrease of the optical band gap.

Based to the Tauc equation at the end of absorption edge region ($\alpha \geq 10^4$ cm^{-1}), the optical energy band gap E_g can be computed via the values of the absorption coefficient [35, 36]:

$$\alpha(h\nu) = A(h\nu - E_g^{\mathrm{opt}})^r, \qquad (16)$$

where A is a constant parameter and depends on the transition probability and $r = 2$ for non-direct transition and $r = 1/$ for the direct transition. For as-prepared and some annealed temperatures at 370 and 380 K
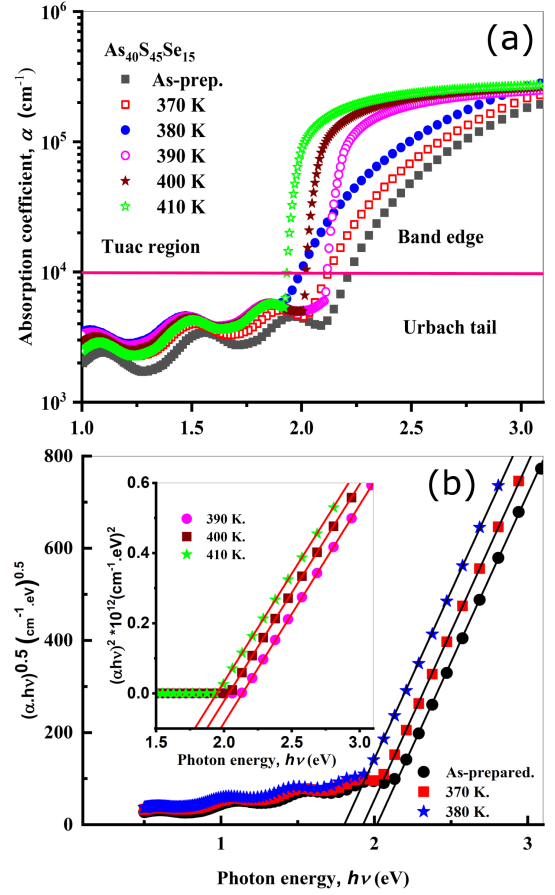

Fig. 4. The dependence of the absorption coefficient on the incident photon energy (a) and the plots of indirect transitions and direct transitions with the photon energy (b) for $As_{40}S_{45}Se_{15}$ thin films annealed at various temperatures.

of $As_{40}S_{45}Se_{15}$ thin films we notice that the indirect transitions are valid and the direct transition is valid for annealed $As_{40}S_{45}Se_{15}$ thin films around and after the inset of crystallization temperatures, namely at 390, 400, and 410 K. Figure 4b shows the $(\alpha h\nu)^{1/2}$ against $h\nu$ for as-prepared and annealed temperatures 370 and 380 K while it shows the $(\alpha h\nu)^2$ against $h\nu$ for annealed temperatures 390, 400, and 410 K. The optical energy band gap E_g of the films was estimated from the intercept of linear portion of each curve for different annealing temperatures with $h\nu$ in the abscissa, i.e. at $(\alpha h\nu)^{1/2} = 0$, $(\alpha h\nu)^2 = 0$, respectively, as presented in Fig. 4b. Additionally, increase in the annealed temperature leads to an increase in the crystallite size. For this reason, the decrease in the band gap energy may be attributed to quantum confinement phenomena.

On the other hand, the absorption coefficient at less than about $\alpha \approx 10^4$ cm^{-1} near the absorption edge depends exponentially on $h\nu$ as follows [37, 38]:

$$\alpha(h\nu) = \alpha_0 \exp\left(\frac{h\nu}{E_e}\right) \qquad (17)$$

TABLE IV

Values of energy gap E_g^{opt} width of localized states E_e and dispersion parameters of the $As_{40}S_{45}Se_{15}$ thin films annealed at various temperatures.

T [K]	E_g^{opt} [eV] E_g^{ind}	E_g^{dir}	E_e [eV]	σ_s	E_d [eV]	E_o [eV]	n_o	ε_o	ε_l	$N/m^* \times 10^{56}$ [m^{-3} kg^{-1}]	$s_o \times 10^{13}$ [m^2]	λ_o [nm]
as-prep.	2.01	–	0.153	0.152	15.45	3.63	2.29	5.25	5.80	2.21	4.16	319.4
370	1.93	–	0.177	0.178	16.69	3.56	2.38	5.69	6.27	2.43	3.71	355.5
380	1.80	–	0.160	0.160	17.66	3.55	2.44	5.97	6.51	3.04	3.36	380.7
390	–	1.97	0.715	0.715	15.17	3.27	2.37	5.63	6.32	3.46	2.88	400.2
400	–	1.88	0.650	0.654	13.74	3.13	2.32	5.39	6.08	3.78	2.47	420.7
410	–	1.79	0.609	0.604	12.60	2.97	2.29	5.24	5.91	3.99	2.12	445.9

where α_o is a constant and E_e is the Urbach energy deduced from plotting $\ln(\alpha)$ versus $h\nu$ as illustrated in Fig. 5. The computed values of E_g and E_e are presented in Table IV. It is clear that the obtained values of E_g decrease with increase of annealed temperature around and after T_c while E_e increases with increase of annealed temperature in the same range. This may be a result of the increase of the lattice parameter and hence the unit cell size. Also the amorphous-crystalline transformations after annealing are responsible for decrease of the film optical gap [9, 20, 30, 39]. Additionally, the steepness parameter σ characterizing the broadening of the optical absorption edge due to electron–phonon or exciton–phonon interactions [40] was also computed for the as-prepared film ($T = 300$ K in this film) and annealed films from the subsequent equation:

$$\sigma_{\mathrm{steepness}} = \frac{k_{\mathrm{B}}T}{E_e}, \qquad (18)$$

where k_{B} is Boltzmann's constant that is equal to 8.617×10^{-5} eV/K. The values of $\sigma_{\mathrm{steepness}}$ for different annealed $As_{40}S_{45}Se_{15}$ thin films are listed in Table IV. It is noticed that the steepness parameter σ has the same trend as the optical band gap.

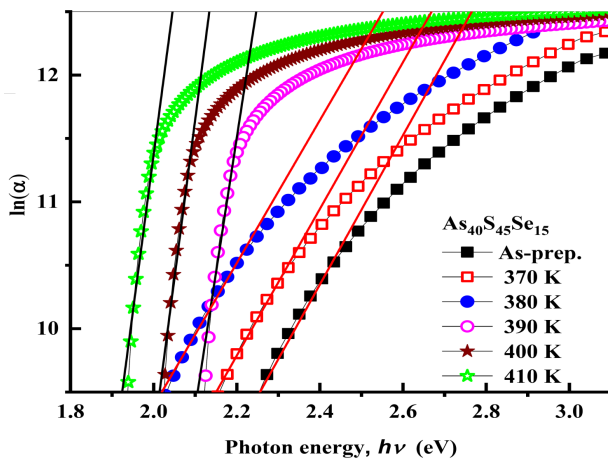Fig. 5. The plot of $\ln\alpha$ vs. photon energy for $As_{40}S_{45}Se_{15}$ thin films annealed at various temperatures.

3.3. Estimation of optical constants

3.3.1. Estimation of refractive index in all transmission spectra

Figure 6a presents the dependence of refractive index on wavelength for as-prepared and different annealed temperatures of thin films under investigation. In the strong absorption spectral region, the values of the refractive index can be fitted using the two-term Cauchy dispersion relationship, $n(\lambda) = a + (b/\lambda^2)$ which can be used to extrapolate the complete overall wavelengths [41]. It is clear that the refractive index increases with annealing temperatures before 390 K and decreases with increasing annealing temperature around and after 390 K, which represents T_c. The values of the Cauchy coefficients a and b are tabulated in Table V. Such a change is attributed to different values of packing density p of the thin films [42, 43], which can be computed from the Lorentz–Lorenz relation [44]:

$$p = \frac{(n^2 - 1)(n_b^2 + 1)}{(n^2 + 1)(n_b^2 - 1)}, \qquad (19)$$

where n_b is the refractive index of bulk $As_{40}S_{45}Se_{15}$. Taking $n_b = 2.841$ and $n = 2.802, 2.814, 2.836, 2.774, 2.743,$ and 2.736 at 500 nm, the values of packing densities are 0.993, 0.995, 0.999, 0.988, 0.982, and 0.980 for the as-prepared film and films annealed at 370, 380, 390, 400, and 410 K, respectively. The as-prepared $As_{40}S_{45}Se_{15}$ film has a minimum packing density, which increases a little at 370 and 380 K. The increase in packing density will lead to a decrease in thickness of $As_{40}S_{45}Se_{15}$ layer. On the other hand, for the annealing temperature at 380 K, the packing density increases to a maximum value. After annealing at around 390, 400, and 410 K, the packing density presents a tendency of decreasing until it reaches a smaller value at 410 K, which is attributed to the presence of cracks in the films at higher annealing temperatures. Furthermore, the decrease in refractive index up to 390 K and beyond for investigated samples may be attributed to the reduction of the number of unsaturated defects, which causes the reduction in the density of localized states in the band structure consequently decreasing the refractive index [45], while the increase occurs due to reverse of this reason.

Values of the Cauchy coefficient parameters (a, b), the electrical conductivity $\sigma_{0,T}$, first order susceptibility $\chi^{(1)}$, third-order susceptibility $\chi^{(3)}$, and non-linear refractive index n_2 for the studied samples.

| Ann. T [K] | Cauchy coefficient | | σ_0 | σ_T | $\chi^{(1)}$ | $\chi^{(3)} \times 10^{-12}$ [esu] | $n_2 \times 10^{-11}$ [esu] |
	a	$b \times 10^5$ [nm^2]					
as-prep.	2.28	13801.2	6.74	–	0.339	2.23	3.67
370	2.38	14462.9	–	26.28	0.373	3.29	5.20
380	2.41	17274.9	–	27.96	0.395	4.15	6.41
390	2.36	18963.3	–	25.76	0.369	3.14	4.99
400	2.30	20750.6	–	26.93	0.350	2.53	4.11
410	2.27	23536.2	–	28.09	0.338	2.21	3.64
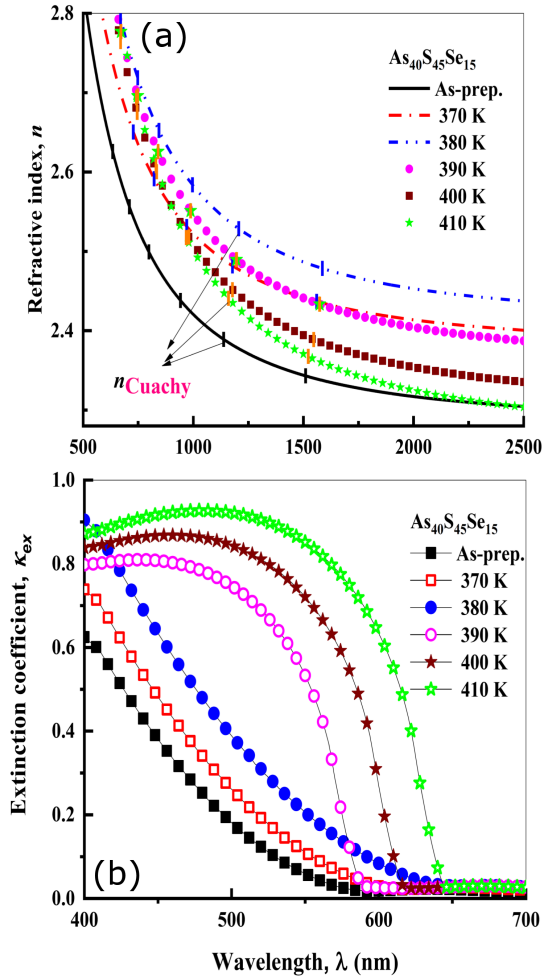
Fig. 6. The spectral dependence of refractive index on the wavelength (a) and the variation of extinction coefficient vs. wavelength (b) for As$_{40}$S$_{45}$Se$_{15}$ thin films annealed at various temperatures.

3.3.2. Estimation of the extinction coefficient

In order to complete the calculations of the optical constants, the values of extinction coefficient, k can be computed from the absorption coefficient and wavelength data via the following relation [29, 46, 47]:

$$k_{\mathrm{ex}} = \varepsilon_0 \alpha \lambda = \frac{\alpha \lambda}{4\pi}. \qquad (20)$$

The values of K_{ex} versus the wavelength for studied thin films are presented in Fig. 6b. It is evidently seen that the extinction coefficient K_{ex} increases with increase of the annealing temperatures. On the other hand, it is noticed that the values of K_{ex} of the thin films decrease with increase of wavelength and becomes very small at longer wavelengths, demonstrating that the thin films under test are highly transparent.

3.4. Estimation of the dielectric constants and dissipation factor

As a function of n and k, the real and imaginary parts of the dielectric constant [48] of the investigated films has also been computed via the subsequent relation:

$$\begin{cases} \varepsilon_r = n^2 - k^2, \\ \varepsilon_i = 2nk. \end{cases} \qquad (21)$$

The real part of the dielectric constant ε_r and real part of complex refractive index, n for studied thin films reveal similar trend at the same range of photon energy, while the imaginary part of the dielectric constant ε_i and imaginary part of complex refractive index k_{ex} reveal a similar trend at the same range of photon energy. Figure 7a, b presents the variation of these two parameters with photon energy.

After that, the quantity frequently used to characterize the optical properties of thin films is called the dissipation factor $(\tan(\delta))$ which can be determined via the subsequent equation [49]:

$$\tan(\delta) = \frac{\varepsilon_i}{\varepsilon_r}. \qquad (22)$$

$\tan(\delta)$ is a measure of loss rate of power of a mechanical mode such as an oscillation in the dissipative system. For example, electric power is lost in all dielectric materials usually in the form of heat [50]. Figure 8 presents the variation of the dissipation factor as a function of photon energy. It is noticed that the dissipation factor increases with increase in both photon energy and annealing temperature of the studied films.
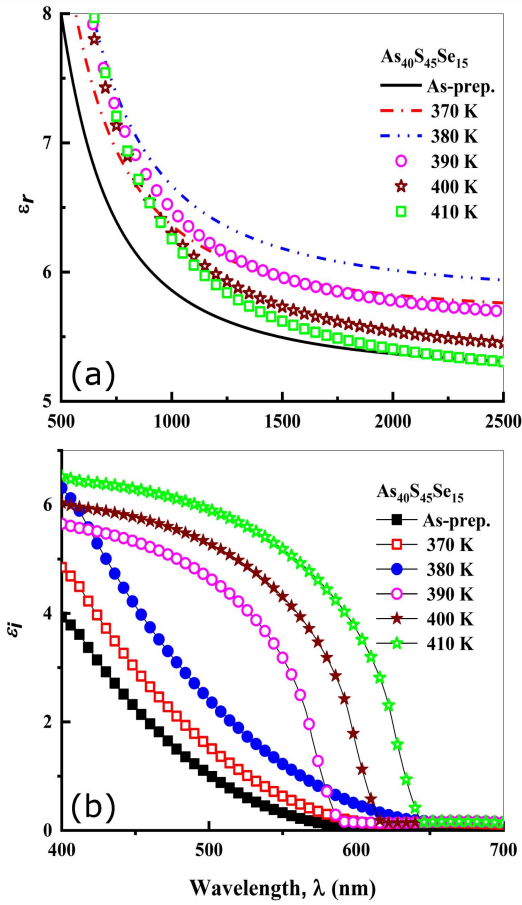
Fig. 7. The variation of real (a) and imaginary (b) dielectric constants on the wavelength for $As_{40}S_{45}Se_{15}$ thin films annealed at various temperatures.
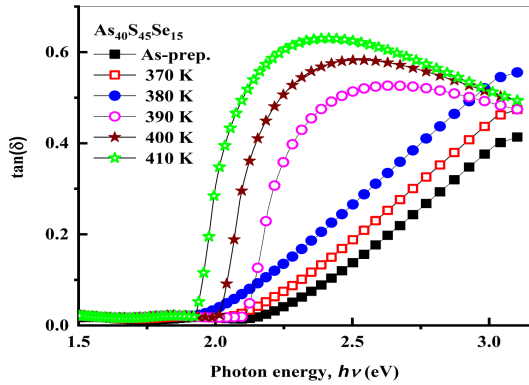

Fig. 8. Variation of dissipation factor on the photon energy for $As_{40}S_{45}Se_{15}$ thin films annealed at various temperatures.

3.5. Determination of the optical and electrical conductivity

The absorption coefficient can be used to compute the optical conductivity σ_{opt} and electrical conductivity σ_{elec} as follows [51]:

$$\begin{cases} \sigma_{opt} = \alpha n c \varepsilon_0 = \dfrac{\alpha n c}{4\pi}, \\ \sigma_{elec} = \dfrac{2\lambda}{\alpha}\sigma_{opt}, \end{cases} \quad (23)$$

where α is the absorption coefficient and c is the light velocity. The variation of optical and electrical conductivity as a function of photon energy is illustrated in Fig. 9a, b. The optical conductivity increases with increase in both photon energy and annealing temperature of the studied films and the electrical conductivity has the same behavior. The increase in optical conductivity at high photon energies may be due to the high absorbance of thin films [52]. On the other hand, the electrical conductivity of studied thin films ($\sigma_{0,T}$) as a function of the band gap energy is given by the subsequent two empirical relations:

$$\sigma_0 = a(bE_g + c) \quad \text{(for as-prepared thin film)}, \quad (24)$$

where a, b, and c are constants of this equation and are equal to 1.259, 0.4663, and 4.462, respectively, and E_g is band gap energy, and

$$\sigma_T = A(BE_g + C) \quad \text{(for annealed thin films)}, \quad (25)$$

where A, B, and C are constants of this equation and are equal to 6.275, -2.058, and 8.160, respectively. These results are listed in Table V.
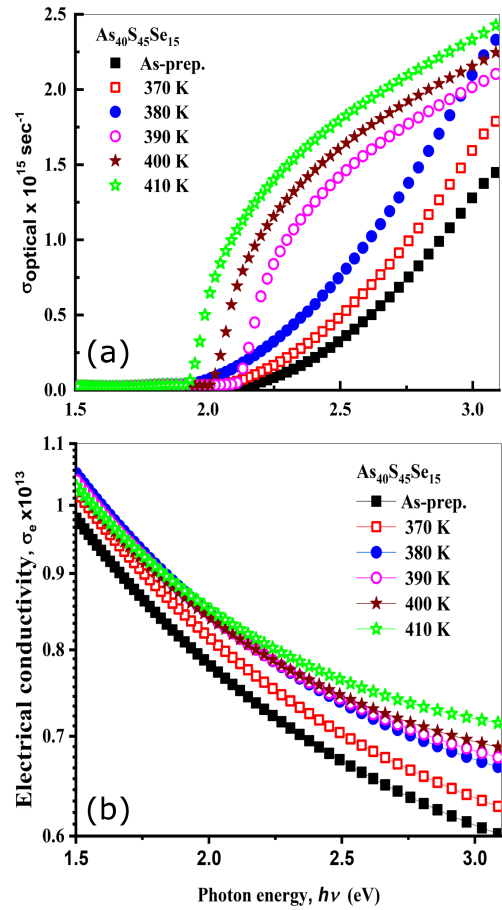

Fig. 9. Dependence of optical (a) and electrical (b) conductivities on the photon energy for $As_{40}S_{45}Se_{15}$ thin films annealed at various temperatures.

3.6. Estimation of the energy-loss functions

Energy absorption by the material which might be due to single electron transitions or to collective effects induced within the solid can be expressed in terms of the volume energy loss functions (VELF) and the surface energy loss functions (SELF) which characterize the probability that fast electrons will lose energy when travelling through the bulk and surface of the material, respectively. The energy-loss functions are attached to the real ε_r and imaginary ε_i parts of the complex dielectric constant by the subsequent relations [53]:

$$\begin{cases} \text{VELE} = \frac{\varepsilon_i^2}{\varepsilon_i^2 + \varepsilon_r^2}, \\ \text{SELE} = \frac{\varepsilon_i^2}{\varepsilon_i^2 + (\varepsilon_r + 1)^2} \end{cases}. \qquad (26)$$

The dependence of both the VELF and SELF on photon energy in the fundamental absorption region for the investigated thin films is illustrated in Fig. 10. It is evident that the two functions increase with increase in the photon energy and annealing temperature of the investigated thin films.
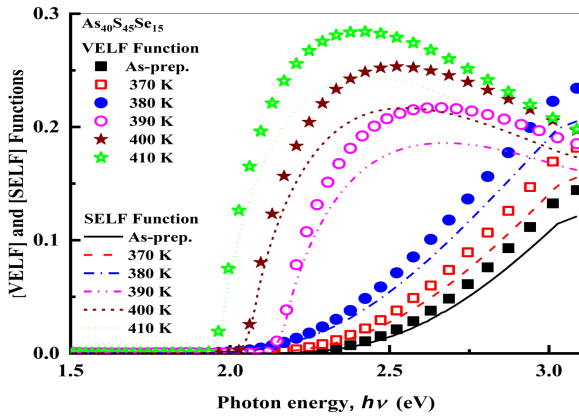

Fig. 10. Dependence of VELF and SELF functions on photon energy in the fundamental absorption region for the investigated samples.

3.7. Estimation of dispersion parameters

Now, the obtained values of the refractive index for $As_{40}S_{45}Se_{15}$ thin films at different annealing temperatures can be fitted for the investigated samples based on the Wemple and DiDomenico model (WDD) in the region from visible to near-infrared by the subsequent equation [23]:

$$(n^2 - 1)^{-1} = \frac{E_o}{E_d} - \frac{1}{E_o E_d} (h\nu)^2, \qquad (27)$$

where $h\nu$ is the photon energy, E_o is the single-oscillator energy, and E_d is the dispersion energy. The values of E_o and E_d are computed from the intercept E_o/E_d and the slope $E_o E_d^{-1}$ of the straight lines of the $(n^2-1)^{-1}$ against $(h\nu)^2$ relation as illustrated in Fig. 11a. The obtained E_o value scales with the energy gap i.e. $E_o \approx 2E_g^{\text{opt}}$ [54]. The changes in E_o values can be attributed to the increase of the localized state width. Also, it is evidently

found that E_o decreases, while E_d value increases with increasing thermal processes before and around T_c, while the opposite occurs after T_c, as tabulated in Table IV. The increase of E_d values with increasing annealed temperatures maybe due to the increase of the rate of diffusion of atoms in the thin films which gives more number of atoms at interstitial sites. This leads to impurity type scattering centres [54].

Moreover, analysis of the $(n^2 - 1)^{-1}$ against $(h\nu)^2$ allows to compute the static refractive index using the subsequent equation

$$n_o = \left(\frac{E_o + E_d}{E_o} \right)^{0.5}. \qquad (28)$$

Thus the values of zero-frequency dielectric constant $\varepsilon_o = n_o^2$ were computed. The values of the n_o and ε_o for all films are presented in Table IV. The values of n_o and ε_o increase with increasing thermal process and $\varepsilon_o < \varepsilon_l$. This behavior may be due to the contribution of charge in the polarization process that occurs inside the material as the light is incident on it [30].

It is necessary to compute some optical constants such as high-frequency dielectric constant ε_l and carrier concentration N/m^* for a better understanding of the optical properties of the studied films. The relation between the optical dielectric constant ε, wavelength λ^2, and n is illustrated in Fig. 11b and given by the subsequent equation [55, 56]:

$$n^2 = \left(\varepsilon_l - r \frac{N}{m^*} \right) \lambda^2. \qquad (29)$$

Here, $r = \frac{e^2}{4\pi c^2 \varepsilon_o}$, where e is an electron charge that equals to $(1.6 \times 10^{19}$ C), ε_l is the lattice dielectric constant, ε_o is the vacuum permittivity $(8.854 \times 10^{-12}$ F/m), N/m^* is the ratio of free carrier concentration N to the effective electron mass m^*. The dependence of n^2 on λ^2 for the different annealing temperatures is linear at longer wavelengths, as presented in Fig. 11b. The values of ε_l were deduced from the intercept with the ordinate $\lambda^2 = 0$ and N/m^* were deduced from slope and are tabulated in Table IV.

On the other hand, the inter-band oscillator wavelength λ_o and the oscillator strength s_o for $As_{40}S_{45}Se_{15}$ thin films at different annealing temperatures can be computed via the single Sellmeier oscillator [57]:

$$(n^2 - 1)^{-1} = \frac{1}{(n_\infty^2 - 1)} \left[1 - \left(\frac{\lambda_0}{\lambda}^2 \right) \right]. \qquad (30)$$

Here, $s_o = \frac{(n_\infty^2 - 1)}{\lambda_o^2}$ is the average oscillator strength. The values of λ_o and s_o for all annealing temperatures thin films were computed from the slope and intercept of the plots $(n^2 - 1)^{-1}$ against λ^{-2} as illustrated in Fig. 11c and are tabulated in Table IV. The values of λ_o and s_o changed with change of the thermal processes. These changes show that the film is suitable to change the refractive index and oscillator parameters by changing annealing temperature [23, 58].
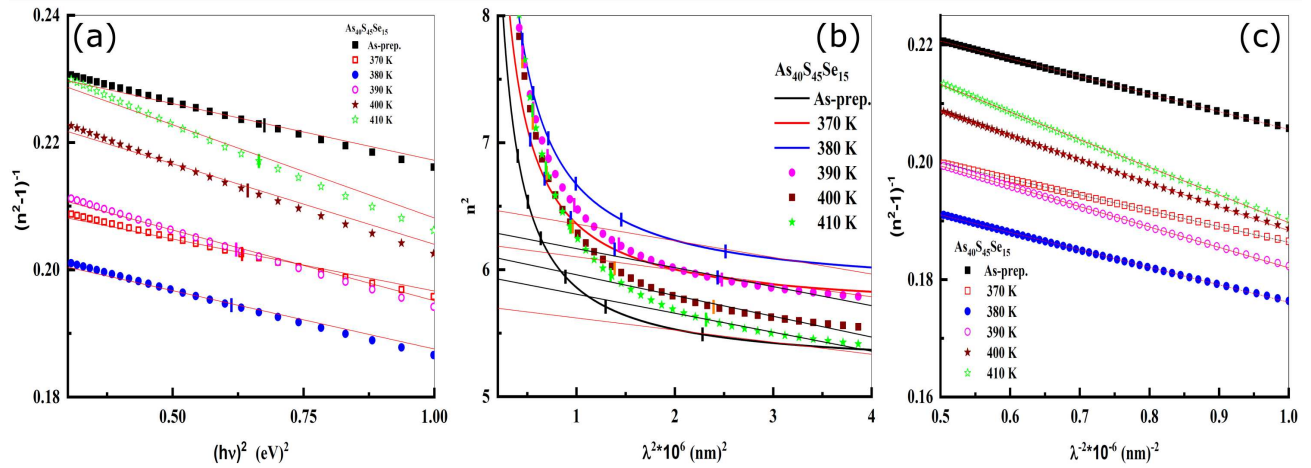
Fig. 11. Plots of $1/(n^2 - 1)$ vs. $h\nu$ (a), n^2 vs. λ^2 (b), and $1/(n^2 - 1)$ vs. λ^{-2} (c) for $As_{40}S_{45}Se_{15}$ thin films annealed at various temperatures.

3.8. Estimation of non-linear refractive index

The nonlinear refractive index n_2 was deduced in terms of Tichy and Ticha relationship [59]. Tichy and Ticha relationship is a combination of Miller's popularized rule and static refractive index computed from WDD model as [41, 59, 60]:

$$n_2 = \frac{12\pi}{n_o}\chi^{(3)}, \tag{31}$$

where $\chi^{(3)}$ is third order non-linear susceptibility and computed from the following relation [61]:

$$\chi^{(3)} = A(\chi^{(1)})^4, \tag{32}$$

where $\chi^{(1)}$ is linear susceptibility which is expressed as

$$\chi^{(1)} = \frac{1}{4\pi}\frac{E_d}{E_o}, \tag{33}$$

where $A = 1.7 \times 10^{-10}$ (for $\chi^{(3)}$ in esu). Therefore, $\chi^{(3)}$ is expressed as

$$\chi^{(3)} = \frac{A}{(4\pi)^4}\left(n_o^2 - 1\right)^4. \tag{34}$$

The value of non-linear refractive index first orders susceptibility, and third-order susceptibility are computed and listed in Table V. It is found that the value of the non-linear refractive index and third-order susceptibility increases with increase of annealing temperatures before, T_c (390 K), namely, for three investigated samples (as-prepared, 370, and 380 K) and the opposite occurs after 390 K. Figure 12a shows the plot of the non-linear refractive index based on the Tichy and Ticha relation versus wavelength. There is another way to deduce the non-linear refractive index which is proposed by Fournier and Snitzer [62] on the basis of linear refractive index n and WDD parameters E_o, E_d in the following relation and shown in Fig. 12b:

$$n_2 = \frac{(n^2 + 2)^2(n^2 - 1)}{48\pi nN}\frac{E_d}{E_o^2}, \tag{35}$$

where N is the density of polarizable constituents which is computed via density/molar volume data. The non-linear refractive index is determined in esu [63, 64]. The density of the system is computed theoretically via the subsequent relation:

$$\rho = \frac{x\rho_{Zn} + y\rho_{Co} + z\rho_O}{100}. \tag{36}$$

From the density data, the molar volume given by

$$V_m = \frac{1}{\rho}\sum_i X_i M_i, \tag{37}$$

where M_i is the molecular weight of the i-th component and X_i is the atomic percentage of the same element in the film. The density and the molar volume are equal to 4.76 g/cm^3 and 1475.6 cm^3/mol, respectively. Figure 12b represents the variation in non-linear refractive index according to Fournier and Snitzer relationship with wavelength. It is clear from Fig. 12b that n_2 increases linearly with n whereas n_2 follows the same trend as n follows with wavelength.

3.9. Estimation of the inter-band transition strength

The inter-band transition strength $J_{cv}(E)$ accounts for the dipole selection rules for the transitions [63, 64]. $J_{cv}(E)$ is proportional to the probability that a transition of an electron between the filled valence band and the empty conduction band with transition energy takes place and is related to complex dielectric constant ε by [63, 64]:

$$J_{cv}(E) = \frac{4\pi m_*^2}{e^2 h^2}\frac{(h\nu)^2}{2}(\varepsilon_r + i\varepsilon_i), \tag{38}$$

where m_* is the mass of the electron and $h\nu$ is the photon energy. $J_{cv}(E)$ is proportional to the transition probability and has units g/cm^3. For computational convenience, we take the prefactor $\frac{4\pi m_*^2}{e^2 h^2}]$ in Eq. (38), whose value in (8.289×10^{-6} g/eV^2) as unity. The two parts of $J_{cv}(E)$ are computed from Eq. (38) and presented in Fig. 13

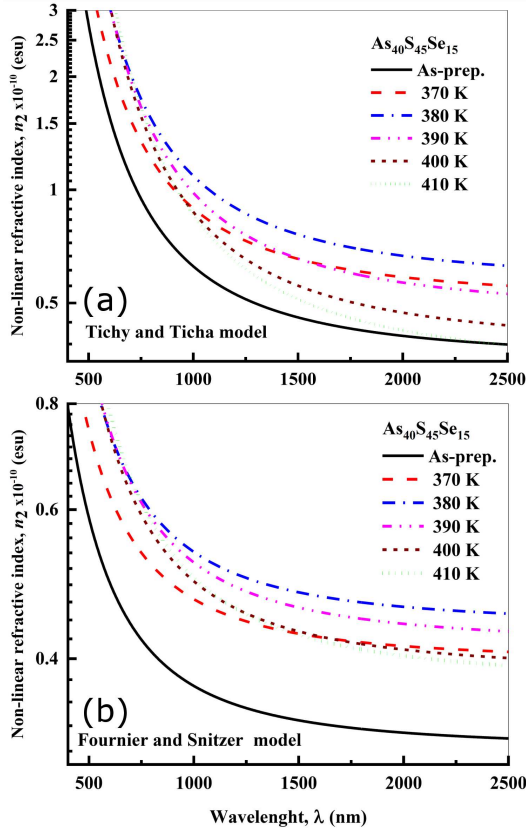Fig. 12. The dependence of non-linear refractive index according to Tichy and Ticha model on the wavelength (a) and according to the Fournier and Snitzer model (b) on the wavelength for $As_{40}S_{45}Se_{15}$ thin films annealed at various temperatures.
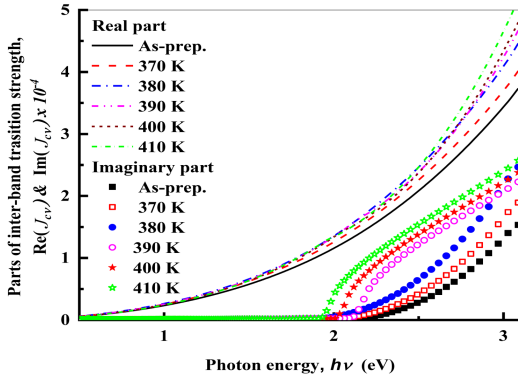

Fig. 13. Plots of the real and imaginary parts of inter-band transition strength as a function of wavelength for $As_{40}S_{45}Se_{15}$ thin films annealed at various temperatures.

that shows inter-band transition strength as a function of the photon energy. It increases with the increasing photon energy and this denotes that the probability of electronic transitions increases with increase of photon energy. The figure shows that the inter-band transition

strength grows significantly when the photon energy is higher than 2 eV and this means that most of the high absorption happens after this value of the energy, which increases excitation of the electron and moves it from the valence band to conduction band. The inter-band transition strength $J_{cv}(E)$ increases with increase in both photon energy and thermal processes but it is shifted towards the lower energies by increasing the temperatures.

4. Conclusions

X-ray diffractogram of the as-prepared and annealed $As_{40}S_{45}Se_{15}$ thin films shows no sharp peaks in the first three films, which ensures the amorphous nature of the samples and then there is emergence of sharp peaks in the last three films and this is evidence of crystallization. Swanepoel's method has been introduced in order to reduce the film thickness, the refractive index, and hence other optical constants. In the range of crystallization area of DSC curve, it is noticed that the results of XRD explain that the crystallinity of the dominant phase $As_2(Se, S)_3$ is improved by increasing the annealing temperature, namely, annealing develops polycrystallinity in the films and an increase in grain size is observed. The optical absorption in the investigated system seems to be of beneficial indirect transition for amorphous thin films and direct transition for annealed crystalline thin films. The optical band gap decreases with increasing annealing temperature around and after T_c. The decrease in the energy band gap may be attributed to quantum confinement phenomena. In addition, the refractive index decreases with increase of annealing temperature. This behavior may be attributed to the lowering of the number of unsaturated defects, which causes a reduction in the density of localized states in the band structure. Additionally, the dispersion parameters such as $E_d, E_o, \varepsilon_o, \varepsilon_l, s_o$, and λ_o are sensitive to the thermal processes. Finally, non-linear refractive index of these thin films has been obtained by using the Tichy and Ticha and the Fournier and Snitzer formulations based on the Wemple–DiDomenico single-oscillator parameters E_o, E_d. The inter-band transition strength $J_{cv}(E)$ for studied thin films was discussed. The interesting thing about this research is that thin films behave differently, whether in the case of X-rays or in the case of optical transitions, making these thin films one of the best promising materials in the future.

References

[1] J. Solis, C.N. Afonso, S. Hyde, N. Barry, P.M. French, *Phys. Rev. Lett.* **76**, 2519 (1996).

[2] J. Coombs, A. Jongenelis, W. van Es-Spiekman, B. Jacobs, *J. Appl. Phys.* **78**, 4906 (1995).

[3] A. Hilton, *J. Non-Cryst. Solids* **2**, 28 (1970).

[4] R. Frerichs, *J. Opt. Soc. Am.* **43**, 1153 (1953).

[5] A. Zakery, S.R. Elliott, *J. Non-Cryst. Solids* **330**, 1 (2003).

[6] V. Shiryaev, C. Boussard-Plédel, P. Houizot, T. Jouan, J.L. Adam, J. Lucas, *Mater. Sci. Eng. B* **127**, 138 (2006).

[7] E.R. Shaaban, M.N. Abd-el Salam, M. Mohamed, M.A. Abdel-Rahim, A.Y. Abdel-Latief, *J. Mater. Sci. Mater. Electron.* **28**, 13379 (2017).

[8] J. Singh, *Optical Properties of Condensed Matter and Applications*, Wiley, 2006.

[9] E. Shaaban, H. Elshaikh, M. Soraya, *Optoelectron. Adv. Mater. Rapid Commun.* **9**, 587 (2015).

[10] V. Takats, A.C. Miller, H. Jain, A. Kovalskiy, S. Kokenyesi, *Thin Solid Films* **519**, 3437 (2011).

[11] E.R. Shaaban, G. Abbady, E.S. Yousef, G.A.M. Ali, S.A. Mahmoud, N. Afify, *Optoelectron. Adv. Mater. Rapid Commun.* **13**, 235 (2019).

[12] E.R. Shaaban, *Mater. Chem. Phys.* **100**, 411 (2006).

[13] E. Shaaban, *Philos. Mag.* **88**, 781 (2008).

[14] J. Manifacier, J. Gasiot, J. Fillard, *J. Phys. E Sci. Instrum.* **9**, 1002 (1976).

[15] R. Swanepoel, *J. Phys. E Sci. Instrum.* **17**, 896 (1984).

[16] E.R. Shaaban, M. El-Hagary, E.S. Moustafa, H.S. Hassan, Y.A.M. Ismail, M. Emam-Ismail, A.S. Ali, *Appl. Phys. A Mater. Sci. Process.* **122**, 1 (2016).

[17] D. Štrbac, S. Lukić, D. Petrović, J. Gonzalez-Leal, A. Srinivasan, *J. Non-Cryst. Solids* **353**, 1469 (2007).

[18] J. Gonzalez-Leal, R. Prieto-Alcon, M. Stuchlik, M. Vlcek, S. Elliott, E. Márquez, *Opt. Mater.* **27**, 147 (2004).

[19] J. Ruíz-Pérez, J. González-Leal, D. Minkov, E. Márquez, *J. Phys. D Appl. Phys.* **34**, 2489 (2001).

[20] E. Yousef, A.E. Adawy, N.E. Koshkhany, E.R. Shaaban, *J. Phys. Chem. Solids* **67**, 1649 (2006).

[21] T. Cardinal, K. Richardson, H. Shim, A. Schulte, R. Beatty, K.L. Foulgoc, C. Meneghini, J. Viens, A. Villeneuve, *J. Non-Cryst. Solids* **256**, 353 (1999).

[22] J.S. Sanghera, V.Q. Nguyen, I.D. Aggarwal, *J. Am. Ceram. Soc.* **79**, 1324 (1996).

[23] S.H. Wemple, M. DiDomenico, *Phys. Rev. B* **3**, 1338 (1971).

[24] M. Kotkata, A. Shamah, M.E. Den, M.E. Mously, *Acta Phys. Hung.* **54**, 49 (1983).

[25] A. Patterson, *Phys. Rev.* **56**, 978 (1939).

[26] M. Dhanam, R. Balasundaraprabhu, S. Jayakumar, P. Gopalakrishnan, M. Kannan, *Phys. Status Solidi A* **191**, 149 (2002).

[27] E.R. Shaaban, A.E. Metawa, A. Almohammedi, H. Algarni, A.M. Hassan, G.A.M. Ali, A. Ashour, *Mater. Res. Express* **5**, 086402 (2018).

[28] S. Venkatachalam, D. Mangalaraj, S.K. Narayandass, *Physica B Condens. Matter* **393**, 47 (2007).

[29] E.R. Shaaban, I. Kansal, S. Mohamed, J.M. Ferreira, *Physica B Condens. Matter* **404**, 3571 (2009).

[30] M.E. Hagary, M. Emam-Ismail, E. Shaaban, A. Al-Rashidi, S. Althoyaib, *Mater. Chem. Phys.* **132**, 581 (2012).

[31] R. Swanepoel, *J. Phys. E Sci. Instrum.* **17**, 896 (1984).

[32] R. Swanepoel, *J. Phys. E Sci. Instrum.* **16**, 1214 (1983).

[33] R. Vahalová, L. Tichý, M. Vlček, H. Tichá, *Phys. Status Solidi A* **181**, 199 (2000).

[34] E.R. Shaaban, A. Almohammedi, E.S. Yousef, G.A.M. Ali, K.F. Chong, A. Adel, A. Ashour, *Optik* **164**, 527 (2018).

[35] J. Tauc, *Amorphous and Liquid Semiconductors*, Springer Science and Business Media, 2012.

[36] G.A.M. Ali, O.A. Fouad, S.A. Makhlouf, *J. Alloys Comp.* **579**, 606 (2013).

[37] R. Urbach, *Phys. Rev.* **92**, 1324 (1953).

[38] E.R. Shaaban, M.Y. Hassaan, G. Moustafa, A. Qasem, G.A.M. Ali, E.S. Yousef, *Optik* **186**, 275 (2019).

[39] A.H. Moharram, *Appl. Surf. Sci.* **143**, 39 (1999).

[40] H. Mahr, *Phys. Rev.* **125**, 1510 (1962).

[41] T.S. Moss, *Optical Properties of Semiconductors*, Butterworth, London 1959.

[42] T. Xie, Y. Wang, C. Liu, L. Xu, *Materials* **11**, 646 (2018).

[43] I. Marozau, A. Shkabko, M. Döbeli, T. Lippert, D. Logvinovich, M. Mallepell, C. Schneider, A. Weidenkaff, A. Wokaun, *Materials* **2**, 1388 (2009).

[44] T. Hübert, U. Beck, H. Kleinke, *J. Non-Cryst. Solids* **196**, 150 (1996).

[45] S.A. Khan, J.K. Lal, A.A. Al-Ghamdi, *Opt. Laser Technol.* **42**, 839 (2010).

[46] D. Gosain, T. Shimizu, M. Ohmura, M. Suzuki, T. Bando, S. Okano, *J. Mater. Sci.* **26**, 3271 (1991).

[47] E.K. Shokr, M. Wakkad, *J. Mater. Sci.* **27**, 1197 (1992).

[48] A. El-Korashy, H. El-Zahed, M. Radwan, *Physica B Condens. Matter* **334**, 75 (2003).

[49] M. El-Nahass, A. Farag, K.A. El-Rahman, A. Darwish, *Opt. Laser Technol.* **37**, 513 (2005).

[50] E. El-Metwally, M. Abou-Helal, I. Yahia, *J. Ovonic Res.* **4**, 20 (2008).

[51] J.I. Pankove, *Optical Processes in Semiconductors*, Courier Corporation, New York 1975.

[52] F. Yakuphanoglu, A. Cukurovali, I. Yilmaz, *Opt. Mater.* **27**, 1363 (2005).

[53] M. El-Nahass, H. Soliman, A. Hendi, *Austral. J. Basic Appl. Sci.* **5**, 145 (2011).

[54] M.A. Abdel-Rahim, M.M. Hafiz, A.Z. Mahmoud, *Solid State Sci.* **48**, 125 (2015).

[55] M.M. Malik, M. Zulfequar, A. Kumar, M. Husain, *J. Phys. Condens. Matter* **4**, 8331 (1992).

[56] N. Mott, E. Davis, R. Street, *Philos. Mag.* **32**, 961 (1975).

[57] A. Walton, T. Moss, *Proc. Phys. Soc.* **81**, 509 (1963).

[58] H.M. Kotb, M. Dabban, A. Abdel-Latif, M. Hafiz, *J. Alloys Comp.* **512**, 115 (2012).

[59] H. Ticha, L. Tichy, *J. Optoelectron. Adv. Mater.* **4**, 381 (2002).

[60] E.R. Shaaban, M.M. Mahasen, M.M. Soraya, E.S. Yousef, S.A. Mahmoud, G.A.M. Ali, H.A. Elshaikh, *J. Am. Ceram. Soc.* **102**, 4067 (2019).

[61] C.C. Wang, *Phys. Rev. B* **2**, 2045 (1970).

[62] J. Fournier, E. Snitzer, *IEEE J. Quant. Electron.* **10**, 473 (1974).

[63] M. Asobe, T. Kanamori, K.I. Kubodera, *IEEE J. Quant. Electron.* **29**, 2325 (1993).

[64] T. Töpfer, J. Hein, J. Philipps, D. Ehrt, R. Sauerbrey, *Appl. Phys. B* **71**, 203 (2000).